Theor. Comput. Fluid Dyn. (2014) 28:409–426
DOI 10.1007/s00162-014-0325-6

ORIGINAL ARTICLE

Mohammad Ali Vakili · Arman Sadeghi · Mohammad Hassan Saidi

Pressure effects on electroosmotic flow of power-law fluids in rectangular microchannels

Received: 2 March 2013 / Accepted: 23 April 2014 / Published online: 17 May 2014

Abstract In this paper, the fully developed electroosmotic flow of power-law fluids in rectangular microchannels in the presence of pressure gradient is analyzed. The electrical potential and momentum equations are numerically solved through a finite difference procedure for a non-uniform grid. A complete parametric study reveals that the pressure effects are more pronounced at higher values of the channel aspect ratio and smaller values of the flow behavior index. The Poiseuille number is found to be an increasing function of the channel aspect ratio for pressure assisted flow and a decreasing function of this parameter for pressure opposed flow. It is also observed that the Poiseuille number is increased by increasing the zeta potential. Furthermore, the results show that an increase in the flow behavior index results in a lower flow rate ratio, defined to be the ratio of the flow rate to that of a Newtonian fluid at the same conditions. Moreover, whereas the flow rate ratio in the presence of an opposed pressure gradient is smaller than that of a favorable pressure force for shear thinnings, the opposite is true for shear-thickening fluids.

Keywords Microfluidics · Electroosmotic flow · Power-law fluids · Flow behavior index

List of symbols

e	Proton charge (C)
E_x	Electric field in the axial direction (Vm^{-1})
f	Friction factor $\left[=2\tau_{w,\mathrm{av}}/\rho u_{\mathrm{HS}}^2\right]$
F	Component of body force vector (Nm^{-3})
$\mathbf{F}$	Body force vector (Nm^{-3})
H	Half channel height (m)
k_{B}	Boltzmann constant (JK^{-1})
m	Flow consistency index ($\mathrm{Pas}^{\mathrm{n}}$)
n	Flow behavior index
n_0	Ion density at neutral conditions (m^{-3})
p	Pressure (Pa)

Communicated by Oleg Zikanov.

M. A. Vakili · A. Sadeghi (✉) · M. H. Saidi
Center of Excellence in Energy Conversion (CEEC), School of Mechanical Engineering, Sharif University of Technology, P.O. Box: 11155-9567, Tehran, Iran
E-mail: armansadeghi@mech.sharif.edu

M. A. Vakili
E-mail: m_a_vakili@mech.sharif.edu

M. H. Saidi
E-mail: saman@sharif.edu

Q	Volumetric flow rate ($m^3\ s^{-1}$)
r	Radial coordinate (m)
R	Channel radius (m)
Re	Reynolds number $\left[= \rho u_{\mathrm{HS}}^{2-n} H^n / m\right]$
t	Time (s)
T	Absolute temperature (K)
u	Axial velocity (ms^{-1})
u_{HS}	Helmholtz–Smoluchowski velocity [Eq. (20)]
u_{PD}	Pressure-driven velocity [Eq. (24)]
$\mathbf{u}$	Velocity vector (ms^{-1})
W	Half channel width (m)
x, y, z	Coordinates (m)
Z	Valence number of ions in solution
Greek symbols	
α	Channel aspect ratio $[= W/H]$
$\dot{\gamma}$	Magnitude of the strain rate tensor (s^{-1})
$\dot{\boldsymbol{\gamma}}$	Strain rate tensor (s^{-1})
Γ	Velocity scale ratio [Eq. (23)]
ε	Fluid permittivity ($CV^{-1}m^{-1}$)
ζ	Zeta potential (V)
K	Dimensionless Debye–Hückel parameter $[= H/\lambda_{\mathrm{D}}]$
K'	Dimensionless Debye–Hückel parameter for circular geometry $[= R/\lambda_{\mathrm{D}}]$
λ_{D}	Debye length (m)
μ	Effective viscosity (Pas)
ρ	Fluid density (kgm^{-3})
ρ_e	Net electric charge density (Cm^{-3})
τ	Stress tensor component (Pa)
$\boldsymbol{\tau}$	Stress tensor (Pa)
φ	Electrostatic potential (V)
Φ	Externally imposed electrostatic potential (V)
ψ	EDL potential (V)
Subscripts	
av	Average
c	Circular
m	Mean
r	Rectangular
w	Wall
0	Reference
Superscripts	
*	Dimensionless variable

1 Introduction

With the advent of microfluidic devices, the need for designing an appropriate pumping system is of considerable importance. Among various techniques such as magnetohydrodynamics, piezoelectrics and electrohydrodynamics [1–3], electroosmosis [4] has been preferred in lab-on-a-chip microfluidic devices. This is due to the fact that electroosmotic pumping systems have much simpler design and easier fabrication. They have also no moving components and possess the capability of precise flow control. Electroosmosis uses the effect of external electrical field, applied along the channel axis, on an ionized solution as a body force to establish a fluid flow through microchannel. As Reuss [5] discovered, the interaction of a surface with an aqueous electrolytic solution usually results in a relative electrostatic charge on the surface known as zeta potential. The charged surface attracts the counterions in the solution toward itself and develops a layer named electric double layer (EDL) which is shown schematically in Fig. 1. Within EDL, there is an excess of counterions to neutralize the surface charge. If an electric field is applied tangentially along the surface, a force will be exerted on the ions within EDL resulting in their motion. Owing to viscous drag, the liquid is drawn by the ions and therefore flows tangent to the surface.

Primary researches on hydrodynamics of electroosmotic flow were carried out by Burgreen and Nakache [6] and Rice and Whitehead [7] for slit and cylindrical capillaries, respectively, assuming low values of the zeta potential. Levine et al. [8] employed an approximation method in dealing with high zeta potentials. More recently, Kang et al. [9] analytically investigated the electroosmotic flow through an annulus under the situation when the two cylindrical walls carry high zeta potentials. Analytical solutions for fully developed

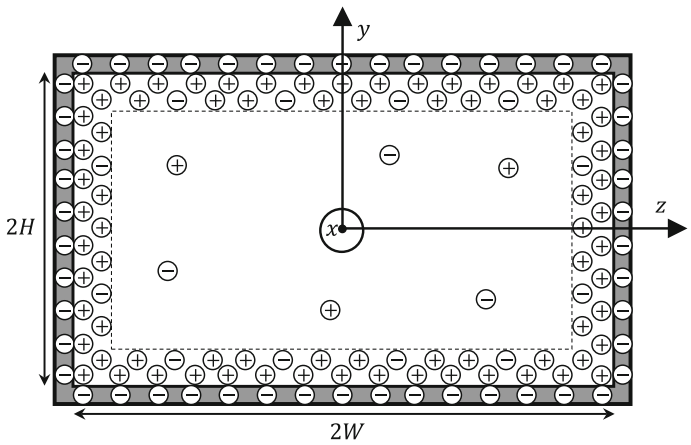

Fig. 1 Schematic of the physical problem along with the coordinate system; EDLs are the regions between the *dashed lines* and the channel wall

electroosmotic flow in rectangular and semicircular microchannels were presented by Yang [10] and Wang et al. [11], respectively.

Since most biofluids encountered in lab-on-a-chip devices show a non-Newtonian behavior, investigating the behavior of such fluids under the influence of the electroosmotic force is highly necessary for an accurate design of lab-on-chip devices. The available literature indicates a growing interest in modeling of the non-Newtonian electroosmotic flow in recent years. One of the first attempts in this context was carried out by Das and Chakraborty who derived analytical solutions for the transverse distributions of velocity, temperature and solutal concentration in electroosmotic flow of power-law fluids through a slit by means of an approximate method [12]. This work was followed by a long line of research works on electroosmotic flow of power-law fluids. Zhao and coworkers [13,14] obtained expressions for the Helmholtz–Smoluchowski electroosmotic velocity of power-law fluids at small and high zeta potentials. In addition, this research group recently developed an approximate velocity distribution for electroosmotic flow of power-law fluids in circular microtubes [15]. By means of the same non-Newtonian model, Vasu and De [16] analyzed the electroosmotic flow in a slit microchannel at high zeta potentials. Bandopadhyay and Chakraborty [17] investigated the ionic size effects on streaming potential and energy transfer efficiency of power-law fluids in narrow confinements. Moreover, there are some other research works being reported in literature on the subject matters of unsteady electroosmotic flow and electroviscous effects on pressure-driven flow of power-law fluids [18–20].

The viscoelastic constitutive equations have also received much attention in electrokinetics studies. Park and Lee [21] devised a simple method based on the concept of the Helmholtz–Smoluchowski velocity to find the volumetric flow rate of viscoelastic electroosmotic flows through microchannels. In addition, they also reported a numerical study on viscoelastic electroosmotic flows through a rectangular microchannel with and without pressure gradient [22]. The electroosmotic flow of viscoelastic fluids through parallel plate microchannels was analytically investigated by Dhinakaran et al. [23].

Some other works have also been reported on a combined electroosmotic and pressure-driven flow. One of the first studies dealing with a combined electroosmotic and pressure-driven flow of non-Newtonian fluids has been carried out by Afonso et al. [24] who derived analytical solutions for the mixed flow of viscoelastic fluids through parallel plates and pipes. They afterward extended their work to the same flow in a parallel plate microchannel with asymmetric zeta potentials [25]. By means of a finite difference-based numerical method, Babaie et al. [26] studied the combined electroosmotic and pressure-driven flow in a slit microchannel using a power-law rheological model. They then extended their work to account for the temperature-dependent effects [27]. Sousa et al. [28] derived analytical solutions for mixed flow of viscoelastic fluids by taking into account the near-wall layer depleted of macromolecules.

In a recent study, the present authors performed a numerical investigation of the fully developed electroosmotic flow of power-law fluids in rectangular microchannels [29]. Here, this work is extended to account for the pressure effects. The existence of the pressure gradient in practical applications may be due to several reasons such as the type of the boundary conditions or use of alternative pumping mechanism in order to reduce the Joule heating effects. For Newtonian fluids, the resulting velocity profile in the presence of pressure would be a linear superposition of the electroosmotic and pressure-driven flow. Nevertheless, for non-Newtonian fluids,

due to their nonlinear nature, such a superposition cannot be applied. Accordingly, an analysis of the mixed electroosmotic and pressure-driven flow of the power-law fluids, performed in this study, is of high importance for design and active control of lab-on-a-chip devices. For fulfilling this duty, a finite difference-based numerical method is employed for solving the nonlinear governing equations in the dimensionless form. After validating the method using available literature data, a complete parametric study is done on the results by special attention to the pressure effects.

2 Problem formulation

Consider the combined electroosmotically and pressure-driven flow of a power-law fluid in a rectangular microchannel with the dimensions given in Fig. 1. The flow is considered to be steady, laminar and fully developed. It is assumed that the liquid, having constant thermophysical properties, contains an ideal solution of fully dissociated symmetric salt. The channel wall is considered to be subject to a constant zeta potential. It is also assumed that the EDLs formed on the channel wall do not overlap. Therefore, since we are dealing with a hydrodynamically fully developed condition, the spatial distribution of the electric charge density can be described by the Boltzmann equation. In addition, in calculating the charge density, it is assumed that the temperature variation over the channel cross section is negligible compared with the absolute temperature; therefore, the charge density field is calculated on the basis of the average temperature.

2.1 Governing equations

The electrical potential distribution within the microchannel is given by the Poisson's equation as

$$\nabla^2\varphi = -\frac{\rho_e}{\varepsilon} \tag{1}$$

where ε is the fluid permittivity and ρ_e is the net electric charge density. The potential φ is due to combination of externally imposed field Φ and EDL potential ψ, that is

$$\varphi = \Phi + \psi \tag{2}$$

For an ideal solution of fully dissociated symmetric salt, the electric charge density is given by [30]

$$\rho_e = -2n_0 eZ \sinh\left(\frac{eZ\psi}{k_B T}\right) \tag{3}$$

where n_0 is the ion density in the bulk solution, Z is the valence of ions, e is the proton charge, T is the absolute temperature and k_B is the Boltzmann constant. For a fully developed flow, $\psi = \psi(y, z)$ and the external potential gradient here is in the axial direction only, that is $\Phi = \Phi(x)$ where x stands for the axial coordinate. For a constant voltage gradient in the x-direction, Eq. (1) becomes

$$\frac{\partial^2\psi}{\partial y^2} + \frac{\partial^2\psi}{\partial z^2} = \frac{2n_0 eZ}{\varepsilon} \sinh\left(\frac{eZ\psi}{k_B T}\right) \tag{4}$$

It has been shown that the temperature effect on the potential distribution is negligible [31]; thus, the potential distribution may be calculated on the basis of the average temperature, T_{av}. Therefore, by taking advantage of the Debye length definition given as $\lambda_D = \left(2n_0 e^2 Z^2/\varepsilon k_B T_{av}\right)^{-1/2}$ and introducing the dimensionless group $\psi^* = eZ\psi/k_B T_{av}$, $y^* = y/H$, $z^* = z/H$, and $K = H/\lambda_D$, Eq. (4) can be non-dimensionalized as

$$\frac{\partial^2\psi^*}{\partial y^{*2}} + \frac{\partial^2\psi^*}{\partial z^{*2}} = K^2 \sinh\psi^* \tag{5}$$

Equation (5) is subject to the following dimensionless boundary conditions

$$\left.\frac{\partial\psi^*}{\partial y^*}\right|_{y^*=0} = 0, \quad \left.\psi^*\right|_{y^*=1} = \zeta^* \tag{6}$$

$$\left.\frac{\partial\psi^*}{\partial z^*}\right|_{z^*=0} = 0, \quad \left.\psi^*\right|_{z^*=\alpha} = \zeta^* \tag{7}$$

where $\alpha = W/H$ is the channel aspect ratio and $\zeta^* = eZ\zeta/k_B T_{av}$ is the dimensionless zeta potential.

The flow field of the power-law fluid is governed by the continuity and Cauchy momentum equations given as

$$\nabla \cdot \mathbf{u} = 0 \tag{8}$$

$$\rho \frac{\mathrm{D}\mathbf{u}}{\mathrm{D}t} = -\nabla p + \nabla \cdot \boldsymbol{\tau} + \mathbf{F} \tag{9}$$

where $\mathbf{u}$ is the velocity vector, ρ is the fluid density, p is the pressure, $\boldsymbol{\tau}$ is the stress tensor and $\mathbf{F}$ is the body force vector. The stress tensor can be related to the strain rate tensor, $\dot{\boldsymbol{\gamma}}$, as

$$\boldsymbol{\tau} = 2\mu(\dot{\gamma})\dot{\boldsymbol{\gamma}} \tag{10}$$

where $\dot{\boldsymbol{\gamma}} = \left(\nabla\mathbf{u} + \nabla\mathbf{u}^T\right)/2$ and $\mu(\dot{\gamma})$ is the effective viscosity with $\dot{\gamma}$ being the magnitude of the strain rate tensor given as [32]

$$\dot{\gamma} = \left(\frac{1}{2}\dot{\boldsymbol{\gamma}} : \dot{\boldsymbol{\gamma}}\right)^{1/2} \tag{11}$$

The effective viscosity for the power-law fluids is given by [32]

$$\mu\left(\dot{\gamma}\right) = m\left(2\dot{\gamma}\right)^{n-1} \tag{12}$$

where m is the flow consistency index and n is the flow behavior index. It is noteworthy that $n < 1$ and $n > 1$ correspond to shear-thinning and shear-thickening fluids, respectively, and by setting $n = 1$ the Newtonian behavior is recovered. Bearing in mind that, at the fully developed conditions, the velocity vector becomes $\mathbf{u} = [u(y, z), 0, 0]$, we come up with the following equations for $\dot{\gamma}$ and μ

$$\dot{\gamma} = \frac{1}{2}\left[\left(\frac{\partial u}{\partial y}\right)^2 + \left(\frac{\partial u}{\partial z}\right)^2\right]^{1/2} \tag{13}$$

$$\mu\left(\dot{\gamma}\right) = m\left[\left(\frac{\partial u}{\partial y}\right)^2 + \left(\frac{\partial u}{\partial z}\right)^2\right]^{\frac{n-1}{2}} \tag{14}$$

From Eqs. (10) and (14), the shear stress components in the axial direction can be written as

$$\tau_{yx} = m\left[\left(\frac{\partial u}{\partial y}\right)^2 + \left(\frac{\partial u}{\partial z}\right)^2\right]^{\frac{n-1}{2}} \frac{\partial u}{\partial y} \tag{15}$$

$$\tau_{zx} = m\left[\left(\frac{\partial u}{\partial y}\right)^2 + \left(\frac{\partial u}{\partial z}\right)^2\right]^{\frac{n-1}{2}} \frac{\partial u}{\partial z} \tag{16}$$

The x-component of the electric body force, generated due to the interaction of the electric charge density in EDL and the electric field, equals $\rho_e E_x$ with $E_x = -\mathrm{d}\Phi/\mathrm{d}x$ denoting the electric field in the axial direction. By substituting ρ_e from Eq. (3), the x-component of the electric body force becomes

$$F_x = -2n_0 eZE_x \sinh\left(\frac{eZ\psi}{k_{\mathrm{B}}T_{\mathrm{av}}}\right) \tag{17}$$

Substituting Eqs. (15), (16), and (17) into Eq. (9) and bearing in mind that $\mathrm{D}\mathbf{u}/\mathrm{D}t = 0$ for a steady fully developed flow, the x-component of the momentum equation becomes

$$\frac{\partial}{\partial y}\left\{m\left[\left(\frac{\partial u}{\partial y}\right)^2 + \left(\frac{\partial u}{\partial z}\right)^2\right]^{\frac{n-1}{2}} \frac{\partial u}{\partial y}\right\} + \frac{\partial}{\partial z}\left\{m\left[\left(\frac{\partial u}{\partial y}\right)^2 + \left(\frac{\partial u}{\partial z}\right)^2\right]^{\frac{n-1}{2}} \frac{\partial u}{\partial z}\right\} - \frac{\mathrm{d}p}{\mathrm{d}x}$$
$$-2n_0 eZE_x \sin\mathrm{h}\left(\frac{eZ\psi}{k_{\mathrm{B}}T}\right) = 0 \tag{18}$$

After expanding the first two terms, Eq. (18) takes the following form

$$\left\{m\left[\left(\frac{\partial u}{\partial y}\right)^2+\left(\frac{\partial u}{\partial z}\right)^2\right]^{\frac{n-3}{2}}\left[n\left(\frac{\partial u}{\partial y}\right)^2+\left(\frac{\partial u}{\partial z}\right)^2\right]\right\}\frac{\partial^2 u}{\partial y^2}+\left\{m\left[\left(\frac{\partial u}{\partial y}\right)^2+\left(\frac{\partial u}{\partial z}\right)^2\right]^{\frac{n-3}{2}}\left[\left(\frac{\partial u}{\partial y}\right)^2+n\left(\frac{\partial u}{\partial z}\right)^2\right]\right\}\frac{\partial^2 u}{\partial z^2}+\left\{2m\,(n-1)\left[\left(\frac{\partial u}{\partial y}\right)^2+\left(\frac{\partial u}{\partial z}\right)^2\right]^{\frac{n-3}{2}}\frac{\partial u}{\partial y}\frac{\partial u}{\partial z}\right\}\frac{\partial^2 u}{\partial y\partial z}-\frac{\mathrm{d}p}{\mathrm{d}x}-2n_0eZE_x\sinh\left(\frac{eZ\psi}{k_\mathrm{B}T}\right)=0 \tag{19}$$

The reference velocity here is considered to be the Helmholtz–Smoluchowski electroosmotic velocity, u_{HS}, which for power-law fluids at small zeta potentials is given as [13]

$$u_{\mathrm{HS}}=n\lambda_{\mathrm{D}}^{\frac{n-1}{n}}\left(-\frac{\varepsilon\zeta E_x}{m}\right)^{\frac{1}{n}} \tag{20}$$

By defining $u^*=u/u_{\mathrm{HS}}$, the momentum equation in the axial direction can be made dimensionless as

$$A_1\left(y^*,z^*,u^*\right)\frac{\partial^2 u^*}{\partial {y^*}^2}+A_2\left(y^*,z^*,u^*\right)\frac{\partial^2 u^*}{\partial {z^*}^2}+A_3\left(y^*,z^*,u^*\right)\frac{\partial^2 u^*}{\partial y^*\partial z^*}=-\left(\frac{n+1}{n}\right)^n\Gamma-\frac{K^{n+1}}{n^n\zeta^*}\sinh\psi^* \tag{21}$$

where $A_1\left(y^*,z^*,u^*\right)$, $A_2\left(y^*,z^*,u^*\right)$ and $A_3\left(y^*,z^*,u^*\right)$ are non-dimensional functions obtained as

$$\begin{aligned}A_1\left(y^*,z^*,u^*\right)&=\left[\left(\frac{\partial u^*}{\partial y^*}\right)^2+\left(\frac{\partial u^*}{\partial z^*}\right)^2\right]^{\frac{n-3}{2}}\left[n\left(\frac{\partial u^*}{\partial y^*}\right)^2+\left(\frac{\partial u^*}{\partial z^*}\right)^2\right]\\A_2\left(y^*,z^*,u^*\right)&=\left[\left(\frac{\partial u^*}{\partial y^*}\right)^2+\left(\frac{\partial u^*}{\partial z^*}\right)^2\right]^{\frac{n-3}{2}}\left[\left(\frac{\partial u^*}{\partial y^*}\right)^2+n\left(\frac{\partial u^*}{\partial z^*}\right)^2\right]\\A_3\left(y^*,z^*,u^*\right)&=2\,(n-1)\left[\left(\frac{\partial u^*}{\partial y^*}\right)^2+\left(\frac{\partial u^*}{\partial z^*}\right)^2\right]^{\frac{n-3}{2}}\frac{\partial u^*}{\partial y^*}\frac{\partial u^*}{\partial z^*}\end{aligned} \tag{22}$$

In Eq. (21), Γ is defined as

$$\Gamma=\frac{u_{\mathrm{PD}}^n}{u_{\mathrm{HS}}^n} \tag{23}$$

where u_{PD} is the maximum velocity of a pressure-driven flow of power-law fluids in a slit microchannel with the height of $2H$ which is expressed as

$$u_{\mathrm{PD}}^n=\left(\frac{n}{n+1}\right)^n\left(-\frac{1}{m}\frac{\mathrm{d}p}{\mathrm{d}x}H^{n+1}\right) \tag{24}$$

The momentum equation is subject to the symmetry, and no slip boundary conditions that in dimensionless form are written as

$$\left.\frac{\partial u^*}{\partial y^*}\right|_{y^*=0}=0,\quad u^*|_{y^*=1}=0 \tag{25}$$

$$\left.\frac{\partial u^*}{\partial z^*}\right|_{z^*=0}=0,\quad u^*|_{z^*=\alpha}=0 \tag{26}$$

Equations (5) and (21) subject to relevant boundary conditions are numerically solved through a finite difference procedure for a non-uniform grid. The method is quite similar to that of our previous study dealing with a purely electroosmotic flow [29], and the details are not presented here in order to save space.

2.2 Flow parameters

Once the potential and velocity fields have been obtained, the parameters of physical interest can be calculated. One of the important parameters of the hydrodynamics is the friction factor given as

$$f = \frac{2\tau_{w,\mathrm{av}}}{\rho u_{\mathrm{HS}}^2} \tag{27}$$

where $\tau_{w,\mathrm{av}}$ is the average wall shear stress that can be obtained as

$$\tau_{w,\mathrm{av}} = -\frac{1}{W+H}\left[\int_0^W \tau_{yx}\big|_{y=H}\,\mathrm{d}z + \int_0^H \tau_{zx}\big|_{z=W}\,\mathrm{d}y\right] \tag{28}$$

Substituting the shear stresses from Eqs. (15) and (16) and replacing the flow parameters with their non-dimensional forms, the friction factor in the form of the Poiseuille number is obtained as

$$fRe = -\frac{2}{1+\alpha}\left\{\int_0^\alpha \left[\left(\frac{\partial u^*}{\partial y^*}\right)^2 + \left(\frac{\partial u^*}{\partial z^*}\right)^2\right]^{\frac{n-1}{2}} \frac{\partial u^*}{\partial y^*}\bigg|_{y^*=1} \mathrm{d}z^* + \int_0^1 \left[\left(\frac{\partial u^*}{\partial y^*}\right)^2 + \left(\frac{\partial u^*}{\partial z^*}\right)^2\right]^{\frac{n-1}{2}} \frac{\partial u^*}{\partial z^*}\bigg|_{z^*=\alpha} \mathrm{d}y^*\right\} \tag{29}$$

where the Reynolds number here is given by $Re = \rho u_{\mathrm{HS}}^{2-n} H^n/m$. Since $\frac{\partial u^*}{\partial z^*}\big|_{y^*=1} = \frac{\partial u^*}{\partial y^*}\big|_{z^*=\alpha} = 0$, the above equation can be simplified as

$$fRe = \frac{2}{1+\alpha}\left\{\int_0^\alpha \left[\left(\frac{\partial u^*}{\partial y^*}\right)^2\right]_{y^*=1}^{\frac{n}{2}} \mathrm{d}z^* + \int_0^1 \left[\left(\frac{\partial u^*}{\partial z^*}\right)^2\right]_{z^*=\alpha}^{\frac{n}{2}} \mathrm{d}y^*\right\} \tag{30}$$

The average value of the effective viscosity at the wall can be evaluated similar to the shear stress invoking Eq. (14). Then, the ratio of the average viscosity at the wall to the viscosity for Newtonian behavior can be written as

$$\frac{\mu_{w,\mathrm{av}}}{\mu_0} = \frac{\frac{m^{1/n}}{\mu_0}\left[\frac{n}{K}\left(-\frac{\varepsilon\zeta E_x}{\lambda_{\mathrm{D}}}\right)^{1/n}\right]^{n-1}}{1+\alpha}\left\{\int_0^\alpha \left[\left(\frac{\partial u^*}{\partial y^*}\right)^2\right]_{y^*=1}^{\frac{n-1}{2}} \mathrm{d}z^* + \int_0^1 \left[\left(\frac{\partial u^*}{\partial z^*}\right)^2\right]_{z^*=\alpha}^{\frac{n-1}{2}} \mathrm{d}y^*\right\} \tag{31}$$

The dimensionless mean velocity is also given as

$$u_m^* = \frac{1}{\alpha}\int_0^\alpha \int_0^1 u^* \mathrm{d}y^* \mathrm{d}z^* \tag{32}$$

The other parameter of interest is the ratio of the volumetric flow rate to a reference flow rate. The reference volumetric flow rate is considered to be that of a Newtonian fluid at the same flow conditions. It can be shown that the flow rate ratio under these conditions is given by

$$\frac{Q}{Q_0} = \frac{u_{\mathrm{HS}}\int_0^\alpha \int_0^1 u^* \mathrm{d}y^* \mathrm{d}z^*}{u_{\mathrm{HS}}|_{n=1}\int_0^\alpha \int_0^1 u^*|_{n=1}\,\mathrm{d}y^* \mathrm{d}z^*} = \frac{u_{\mathrm{HS}}}{u_{\mathrm{HS}}|_{n=1}}\frac{u_m^*}{u_m^*|_{n=1}} = \frac{\mu_0}{m^{1/n}} n\left(-\frac{\varepsilon\zeta E_x}{\lambda_{\mathrm{D}}}\right)^{\frac{1-n}{n}} \frac{u_m^*}{u_m^*|_{n=1}} \tag{33}$$

3 Method validation

The validation of the results is started with a grid dependency analysis of the Poiseuille number values in Table 1. As seen, there is not any significant change in the results when the grid system 500 × 500 is switched to 600 × 600. More precisely, the maximum difference between the results obtained utilizing these grid systems is nearly 0.001 %. Hence, it can be concluded that using 500 × 500 grid points results in sufficiently grid-independent results, especially because high values of K are considered in the grid dependency analysis.

Besides the grid dependency analysis, a comparison with benchmark data is needed for validation of the numerical method. Along this line, the results are compared with existing literature data at two limiting cases. The velocity profile across the channel height at the center of microchannel, that is $z = 0$, is compared with those reported by Babaie et al. [26]. Since this work is dealing with a slit microchannel, a large aspect ratio of $\alpha = 50$ is considered here. Figure 2 shows the comparison for two different values of Γ and, as seen, reveals a good agreement between the results. The Poiseuille numbers are also compared with those obtained from the analytical velocity distribution given by Dutta [33] for purely electroosmotic flow of Newtonian fluids. Since this study assumes applicability of the Debye–Hückel linearization, Eqs. (5) and (21) are changed by considering $\sinh \psi^* \approx \psi^*$ in order to make a reasonable comparison. In addition, the pressure gradient is set to zero by considering $\Gamma = 0$ in Eq. (21). The comparison, which is provided in Table 2, shows a good agreement between the results.

4 Results and discussion

It was shown that five dimensionless parameters including the channel aspect ratio, the dimensionless Debye-Hückel parameter, the dimensionless zeta potential, the flow behavior index, and the velocity scale ratio are

Table 1 Grid dependency of the Poiseuille number values, considering $\alpha = 2$, $\zeta^* = 1$ and $\Gamma = 0.5$

Number of grid points	$K = 100$		$K = 1000$	
	$n = 0.8$	$n = 1.2$	$n = 0.8$	$n = 1.2$
100 × 100	100.1277	420.4462	627.5320	6,667.8994
200 × 200	100.0913	420.4062	627.0688	6,666.4863
300 × 300	100.0850	420.4006	626.9887	6,666.2989
400 × 400	100.0828	420.3989	626.9614	6,666.2423
500 × 500	100.0818	420.3982	626.9489	6,666.2183
600 × 600	100.0813	420.3978	626.9422	6,666.2060

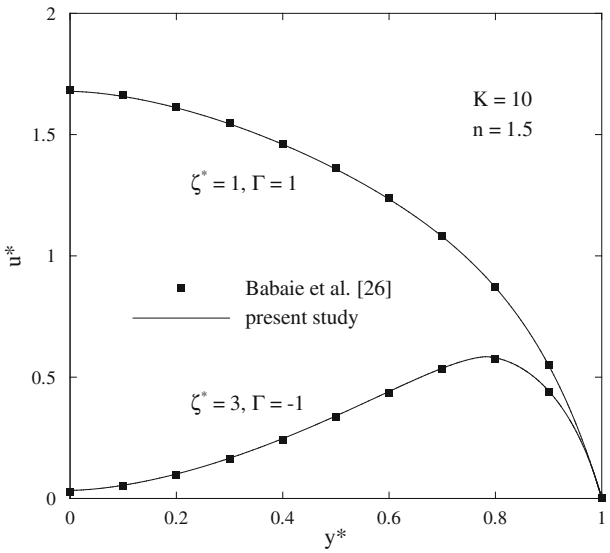

Fig. 2 Comparison between the velocity profiles at the channel center obtained in the present study against those reported by Babaie et al. [26] for a parallel plate channel

Table 2 Comparison of the Poiseuille number values for a purely electroosmotic flow of a Newtonian fluid by assuming the validity of the Debye–Hückel linearization

K	$\alpha = 1$		$\alpha = 2$	
	Present study	Dutta [33]	Present study	Dutta [33]
5	8.72637	8.72636	9.15076	9.15074
10	18.72674	18.72676	19.15125	19.15117
50	98.726308	98.72676	99.15185	99.15117
100	198.72551	198.72676	199.15286	199.15117
500	998.71644	998.72676	999.16435	999.15117

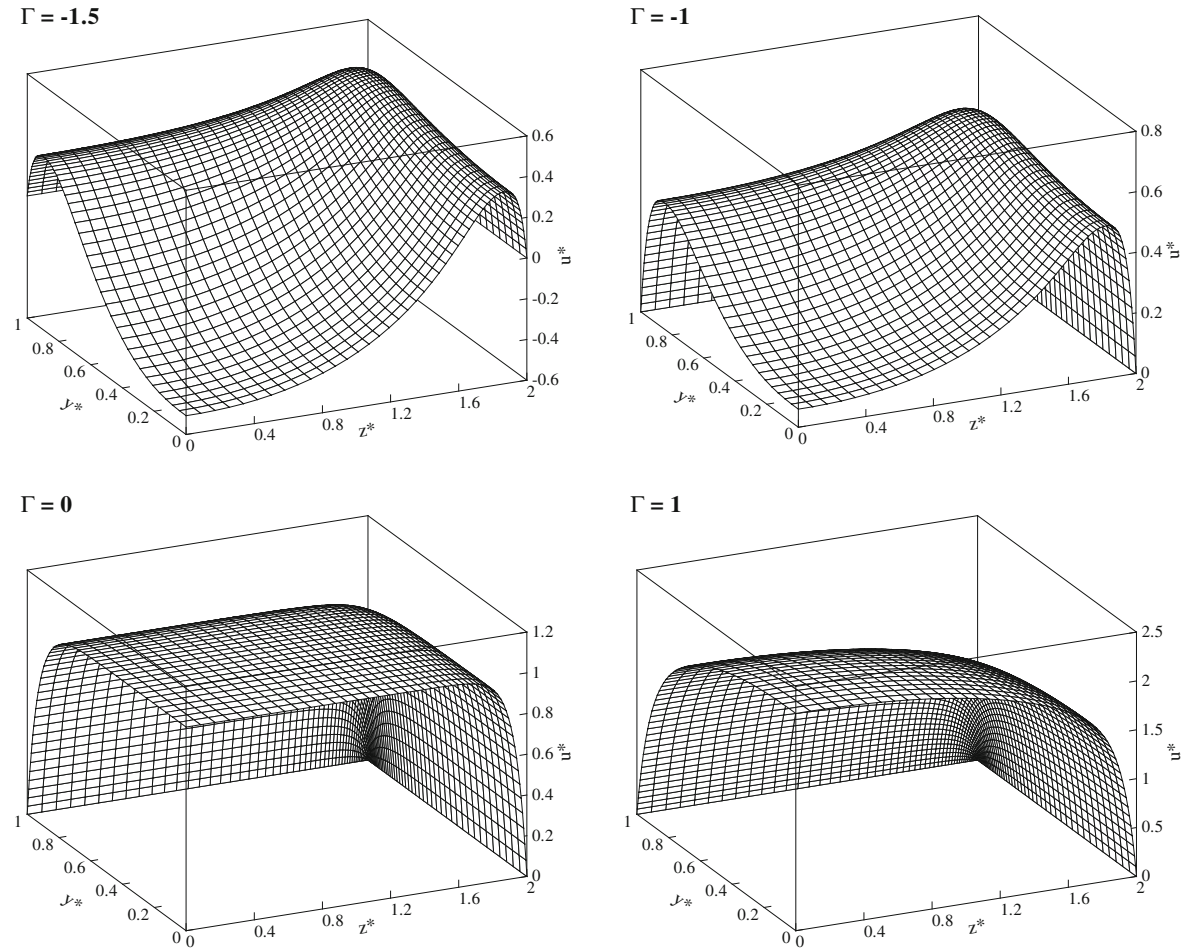

Fig. 3 Non-dimensional velocity distribution at different values of Γ, while keeping $\alpha = 2$, $K = 10$, $\zeta^* = 1$, and $n = 0.7$

the main parameters governing the fully developed electroosmotically and pressure driven flow of power-law fluids in rectangular microchannels. In this section, their interactive effects on the desired flow characteristics such as the velocity distribution, the mean velocity, the flow rate ratio, the Poiseuille number, and the viscosity ratio are being investigated. In presenting the relevant results for the viscosity and flow rate ratios, it is assumed that $\mu_0 = A_0$ Pas and $m = A_0$ Pas^n, thereby considering the numerical values of the flow consistency index and the Newtonian fluid viscosity to be the same. This results in the appearance of the dimensional parameter $\varepsilon\zeta E_x/A_0\lambda_D$ with the units of Pa in the analysis.

Figures 3 and 4 show the dimensionless velocity distribution at different values of Γ for $n = 0.7$ and $n = 1.3$, while keeping $\alpha = 2$, $K = 10$ and $\zeta^* = 1$. The value of the dimensionless Debye–Hückel parameter equal to 10 implies that EDLs are limited to small regions close to the walls and a significant portion of the channel cross section is outside the EDLs. Accordingly, the electric body force is limited to the near-wall

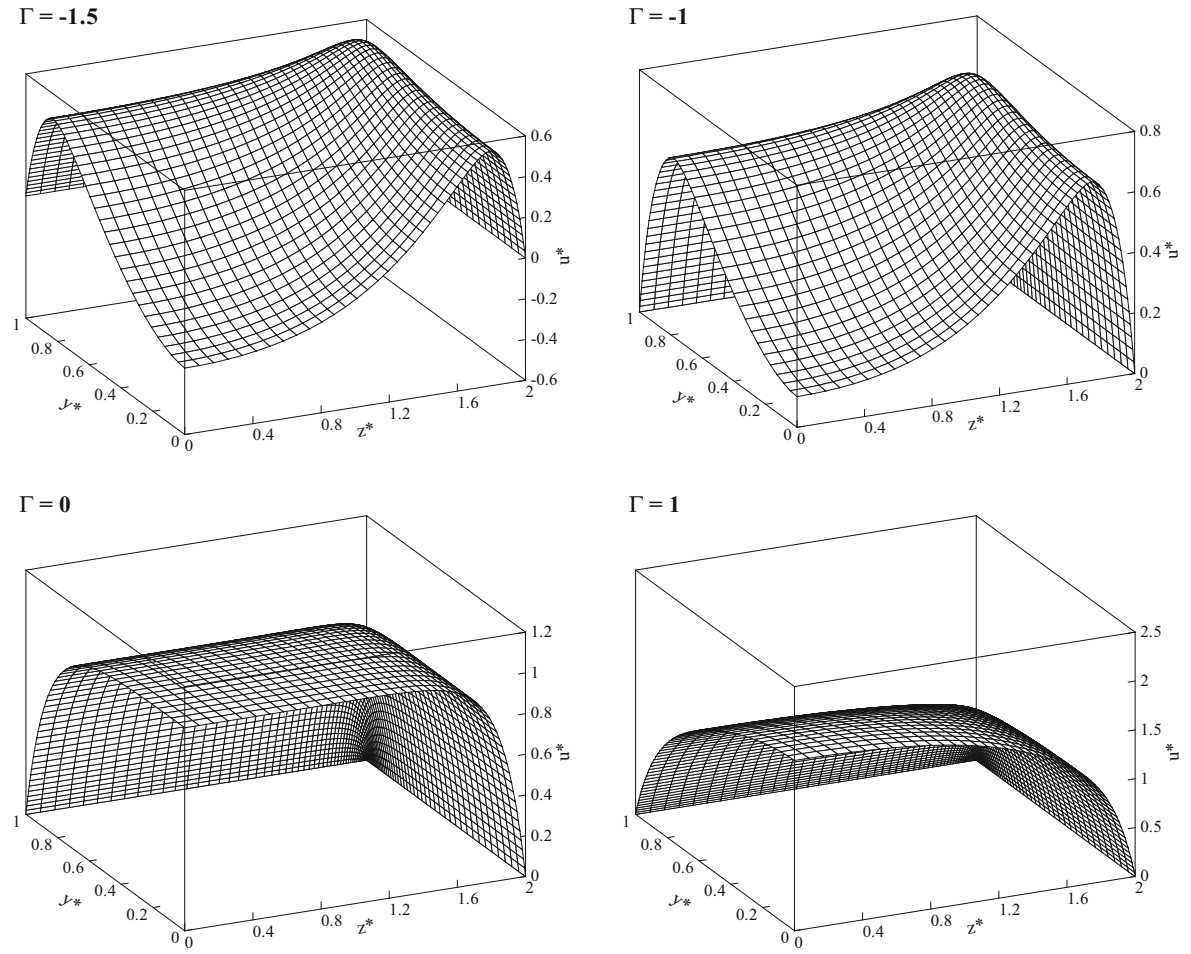

Fig. 4 Non-dimensional velocity distribution at different values of Γ, while keeping $\alpha = 2$, $K = 10$, $\zeta^* = 1$, and $n = 1.3$

regions leading to a nearly slug flow velocity profile in the absence of the pressure gradient, as observed in both Figs. 3 and 4. When a pressure gradient is applied to an electroosmotically driven system, the resultant velocity profile is a combination of both purely electroosmotic and Poiseuille flows. Therefore, the velocity distribution for pressure assisted flow, represented by $\Gamma = 1$, shows both a maximum value at centerline which is related to Poiseuille flow and sharp gradients at the walls which are inherited from electroosmotic flow. For $\Gamma = -1$, the velocity distribution attains its maximum value at a point close to the channel apex and reaches a local minimum at centerline as a result of opposed pressure. The velocity profile for $\Gamma = -1.5$ reveals that, in the presence of a significant opposed pressure, reverse flow may occur near centerline. Such a reverse flow usually occurs in electroosmotic flow between two reservoirs in order to retain the mass conservation.

In Fig. 5, the non-dimensional velocity profile along the channel height at the channel center, that is at $z = 0$, is plotted at different values of Γ, n and α. It can be seen that, in the case of pressure assisted flow, the shear-thinning fluids reach higher velocities in comparison with the shear thickenings. The reason is that a shear-thinning fluid presents smaller viscosities at the wall, resulting in a lower resistance to flow and a higher velocity. In the case of adverse pressure gradient, the dimensionless velocity is greater for shear-thickening fluids compared with the shear thinnings some distance away from the wall, whereas the opposite is seen in the wall vicinity. The fact that u^* is higher for shear-thickening fluids away from the wall should not lead one to the conclusion that these fluids reach higher velocities compared with the shear thinnings. As reported by Zhao et al. [13], the Helmholtz–Smoluchowski velocity, used for non-dimensionalization of the velocity, is several times higher for a shear-thinning fluid than a shear-thickening fluid, and therefore, the velocity of the former is higher even in the presence of an opposed pressure gradient. The graphs also show that the location of the maximum velocity shifts to the channel center by increasing n. The reason is that the fluid with a higher

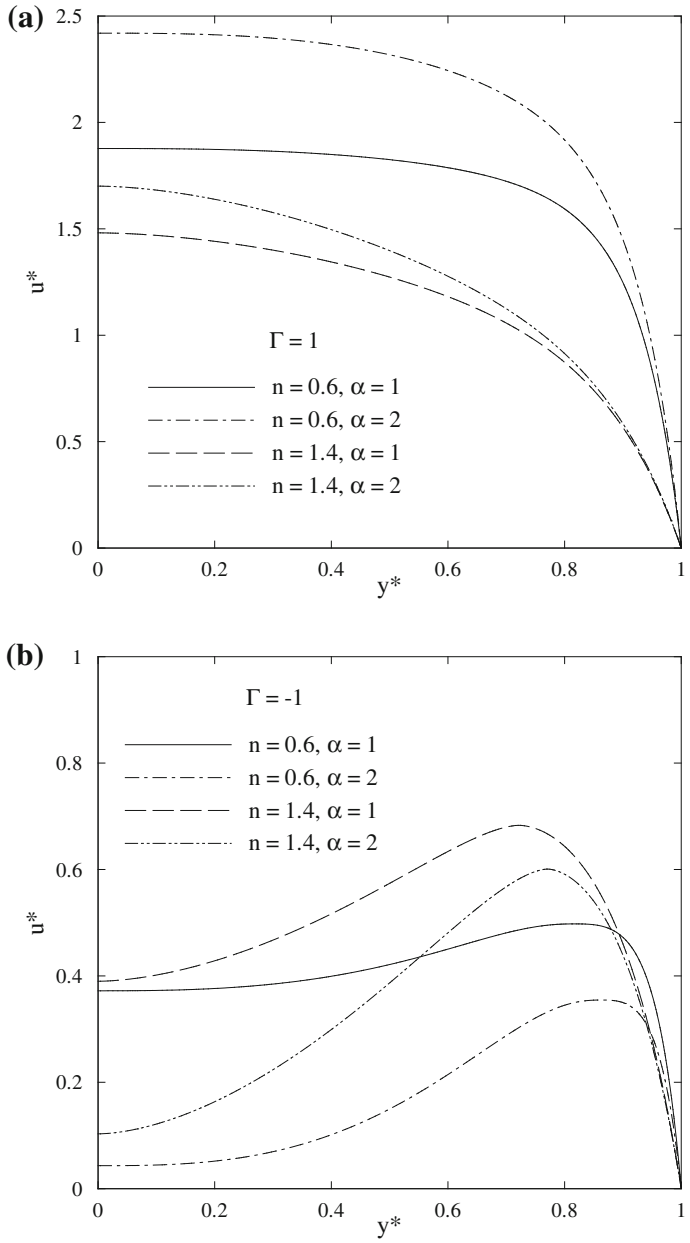

Fig. 5 Velocity profile across the channel height at the channel center for **a** favorable pressure gradient **b** adverse pressure gradient, while keeping $K = 10$ and $\zeta^* = 1$

n shows more resistance against the pressure gradient. Moreover, it is observed that for a positive Γ, a larger aspect ratio leads to higher velocities, whereas the contrary is right for a negative value of this parameter. In other words, the pressure effects are more pronounced for larger aspect ratios. This is because as α increases the distance between the two vertical walls is increased for a given channel height, resulting in smaller surface effects in the core flow and, in turn, paving the way for higher effects of the pressure forces.

The dependency of the Poiseuille number on the channel aspect ratio is illustrated in Fig. 6 for both cases of favorable and adverse pressure gradient. For pressure assisted flow, the Poiseuille number is an increasing function of α, irrespective of the flow behavior index. The reason is that by increasing α, the pressure effects increase resulting in higher velocities and higher velocity gradients near the wall and ultimately higher stresses and higher Poiseuille number. Due to the opposite effect of the channel aspect ratio on the velocity field, an increase in this parameter is accompanied by a smaller fRe for $\Gamma = -1$. The figure further reveals that the

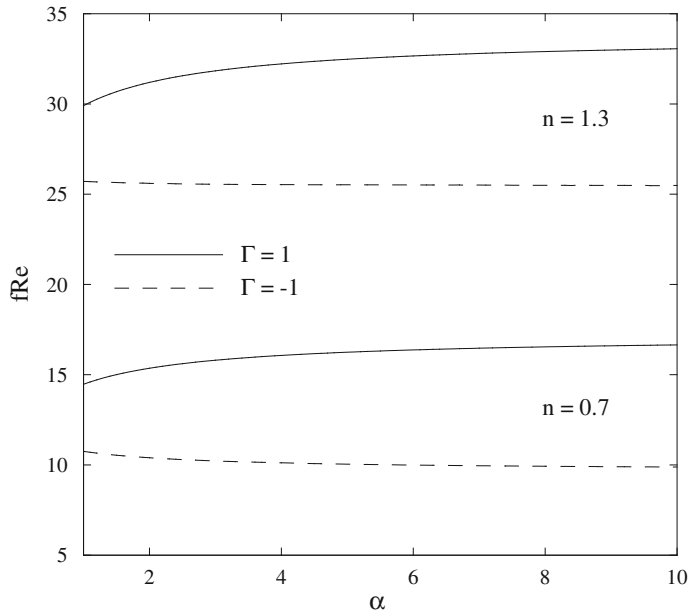

Fig. 6 The dependency of the Poiseuille number on the channel aspect ratio at different values of n and Γ, while keeping $K = 10$ and $\zeta^* = 1$

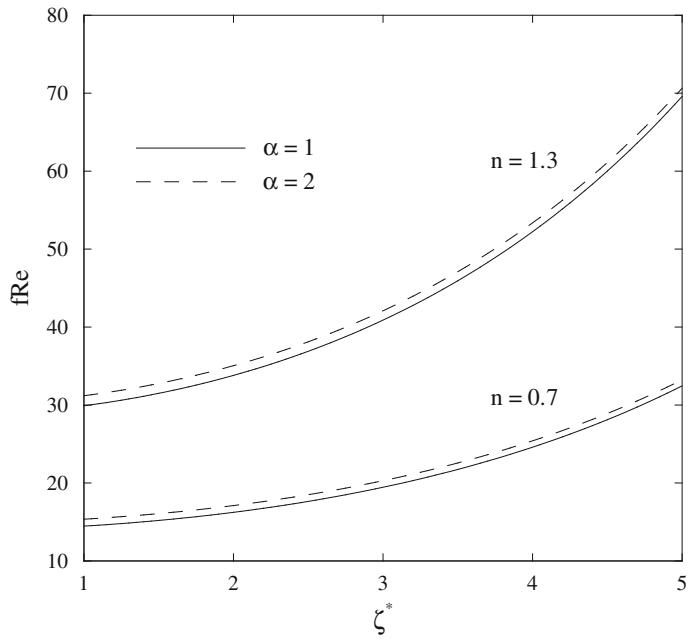

Fig. 7 Effect of the dimensionless zeta potential on the Poiseuille number at different values of n and α, while keeping $K = 10$ and $\Gamma = 1$

Poiseuille number of the pressure opposed flow is lower than that of the case with favorable pressure gradient. This is expected as a higher value of Γ leads to higher driving forces, resulting in higher velocity gradients near the wall.

Figure 7 shows the variations of the Poiseuille number with the dimensionless zeta potential for the pressure assisted flow at different values of n and α. As seen, the Poiseuille number is an increasing function of ζ^*. By increasing ζ^*, the electrical body force within the EDL increases leading to sharper velocity gradients near the wall and consequently a higher Poiseuille number. It is also seen that the fluid with a larger n has a higher Poiseuille number because of higher viscosities at the wall.

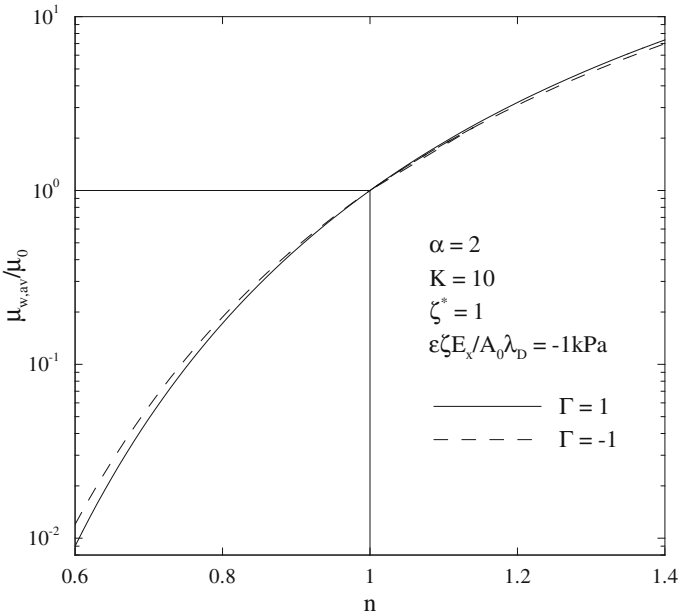

Fig. 8 Viscosity ratio versus the flow behavior index at two different values of Γ

The dependency of the viscosity ratio on the flow behavior index is investigated in Fig. 8. The parameter $\varepsilon\zeta E_x/A_0\lambda_D$ is fixed at -1kPa, a reasonable value for a typical electroosmotic application. As expected, the viscosity ratio increases by increasing n. For shear-thickening fluids, the viscosity ratio is higher for the pressure assisted flow, whereas the reverse is right for shear thinnings. This difference comes from different rheological behaviors of these fluids. The viscosity of a shear-thinning fluid is decreased by increasing the shear rate. Hence, when an opposed pressure gradient is switched to a favorable one, the viscosity at the wall is decreased because of increasing the velocity gradient at the wall. Obviously, the opposite of the above-mentioned explanation is true for the shear-thickening fluids.

The variations of the dimensionless mean velocity with the flow behavior index at different values of Γ and α are given in Fig. 9. The figure reveals that for the case with favorable pressure gradient, the dimensionless mean velocity decreases with increasing n, whereas the opposite is true for the case with an adverse pressure gradient. It should be noted that the Helmholtz–Smoluchowski electroosmotic velocity, used for non-dimensionalization of velocity, itself is a decreasing function of n. Thus, although from Fig. 9, one can conclude that the mean velocity of the pressure assisted flow is also decreased with increasing n, nothing can be said for that of the pressure opposed flow. It can also be concluded from this figure that the pressure effects are more predominant at smaller values of n.

The effect of the dimensionless Debye–Hückel parameter on the dimensionless mean velocity is shown in Fig. 10. The figure shows that for shear-thickening fluids, u_m^* is an increasing function of K. For shear thinnings, increasing K up to $K \cong 10$ results in higher values of u_m^* and further increase will result in an opposite trend. Note that this decrease is only observed in u_m^* and not in the mean velocity itself. In fact, assuming $n = 0.7$, increasing K from 10 to 1000 results in about 7 times increase in the Helmholtz–Smoluchowski velocity. This means that although u_m^* is decreased a little in this range, u_m is increased significantly, and therefore, it is always an increasing function of K. It is also observed in Fig. 10 that the effects of n and K on the dimensionless mean velocity decrease at higher values of the latter. At high values of the dimensionless Debye–Hückel parameter, EDL is restricted to a thin layer near the wall and a pluglike velocity is formed which is not significantly changed by variations of n and K.

Figure 11 depicts u_m^* versus α at different values of n and Γ. The Debye–Hückel parameter and the dimensionless zeta potential are fixed at 10 and 1, respectively. The figure reveals that for the case with a favorable pressure gradient, the dimensionless mean velocity increases by increasing the aspect ratio, while the opposite trend is seen for the case with an adverse pressure gradient. As stated before, these trends are due to higher effects of the pressure force at higher values of α.

It was previously observed that the dimensionless mean velocity is not a convenient tool for studying the variations of the velocity with n because of the dependence of the Helmholtz–Smoluchowski velocity on this

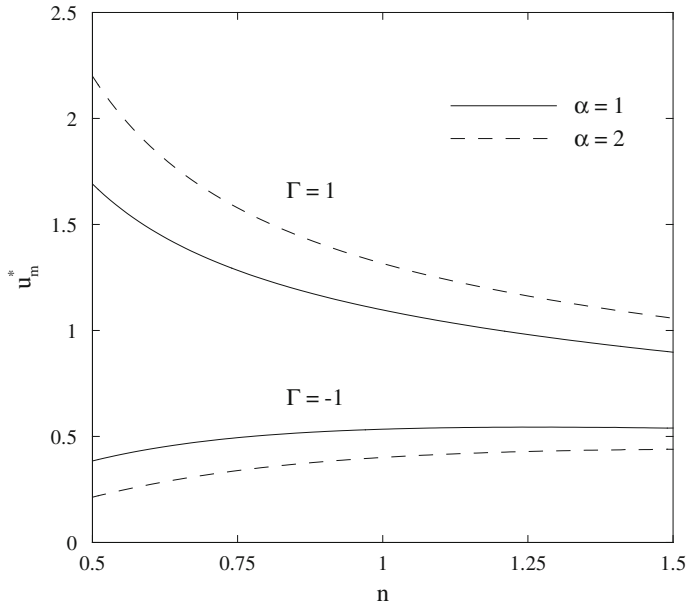

Fig. 9 Effect of the flow behavior index on the dimensionless mean velocity at different values of α and Γ, while keeping $K = 10$ and $\zeta^* = 1$

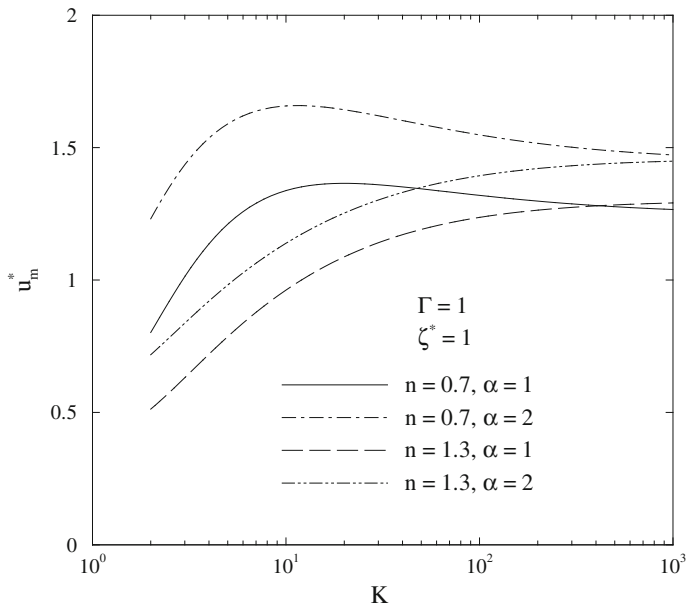

Fig. 10 Dimensionless mean velocity versus the dimensionless Debye–Hückel parameter at different values of n and α

parameter. Unlike u_m^*, the flow rate ratio is an efficient tool for this purpose. The dependency of the flow rate ratio on the flow behavior index is illustrated in Fig. 12. The parameter $\varepsilon\zeta E_x/A_0\lambda_D$ is again fixed at -1 kPa. It is observed that the flow rate is a decreasing function of the flow behavior index regardless of Γ and α. This is because of increasing the resistance against flow at higher values of n as a result of higher viscosities at the wall. This figure also shows that whereas the flow rate ratio in the presence of an opposed pressure gradient is smaller than that of a favorable pressure force for shear thinnings, this trend is reversed for shear-thickening fluids. This may be attributed to higher resistances of the shear thickenings against pressure.

The last part of this section is devoted to the comparison of the present results with those of a circular microchannel. Since the mixed flow of the power-law fluids in circular microchannels has not already been reported in the literature, we only limit the comparison to the purely electroosmotic flow. It has been shown

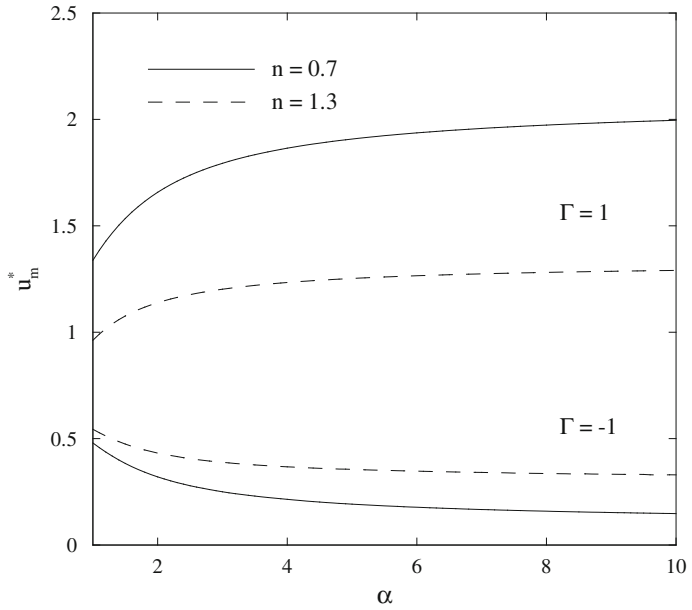

Fig. 11 Effects of the channel aspect ratio on the dimensionless mean velocity at different values of n and Γ, while keeping $K = 10$ and $\zeta^* = 1$

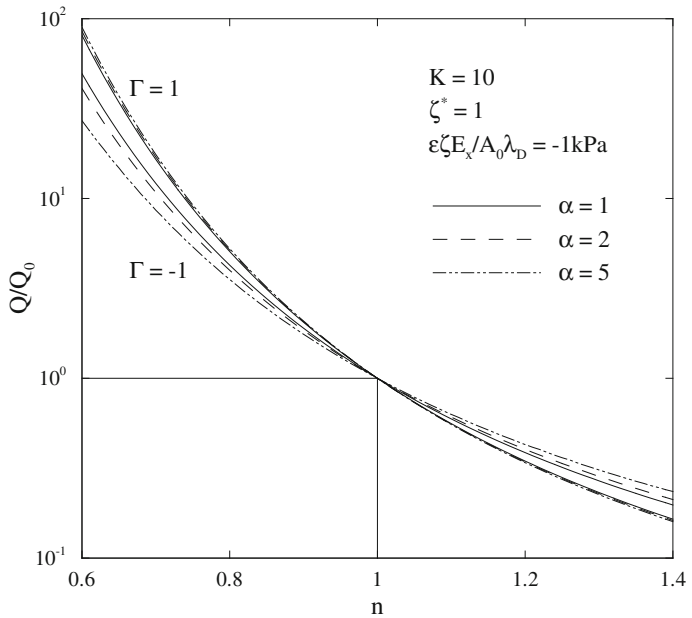

Fig. 12 Flow rate ratio Q/Q_0 versus the flow behavior index at different values of Γ and α

that the dimensionless velocity profile for electroosmotic flow of power-law fluids in a circular microchannel is given as [34]

$$u^*\left(r^*\right) = \frac{K'}{n}\int_{r^*}^{1}\left[\frac{I_1(K'r^*)}{I_0(K')}\right]^{\frac{1}{n}} \mathrm{d}r^* \tag{34}$$

where K' is the ratio of the channel radius, R, to the Debye length and $r^* = r/R$ is the dimensionless radial coordinate. For a reasonable comparison, we assume the same values of the channel cross-sectional area and

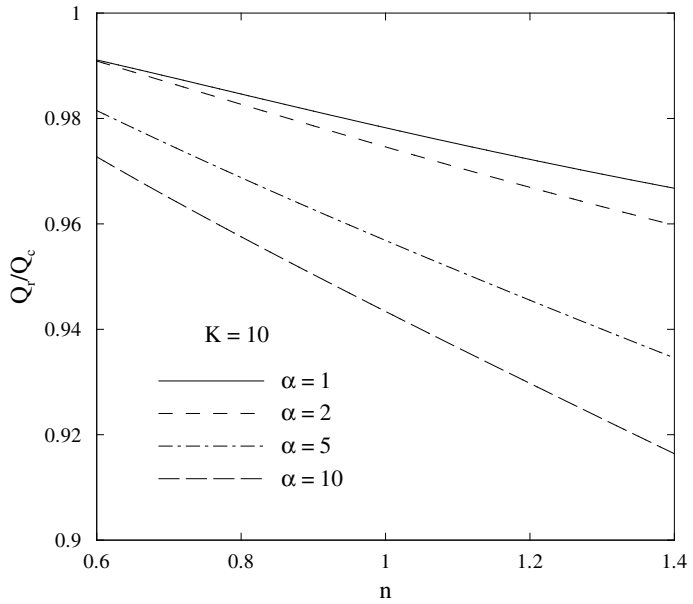

Fig. 13 Flow rate ratio Q_r/Q_c as a function of n at different values of α

the Debye length for both geometries. Under these conditions, K' is related to K and α as

$$K' = 2K\sqrt{\frac{\alpha}{\pi}} \tag{35}$$

After integrating Eq. (34) over the channel cross section, the flow rate ratio of the two geometries, Q_r/Q_c, can be obtained. Since Eq. (34) is derived by applying the Debye–Hückel linearization, the results of the rectangular geometry are also obtained by considering this approximation. Fig. 13 illustrates the variation of the flow rate ratio with respect to the flow behavior index at different values of α. It is observed that for all value of the flow behavior index and the channel aspect ratio, the flow rate is higher for the circular geometry. Moreover, the flow rate ratio is a decreasing function of n. The physical mechanisms behind these variations are explained in the following. The flow rates of the two geometries would be the same if the velocity profile was uniform, because of the equality of the channel areas. Since the fluid reaches the Helmholtz–Smoluchowski velocity away from the wall, the difference in the flow rates therefore arises from the reduction in velocity within EDL. Accordingly, the flow rate of the duct with a larger perimeter will be smaller. It can be shown that the ratio of the rectangular channel perimeter to that of the circular duct with the same channel area becomes $(1+\alpha)/\sqrt{\pi\alpha}$. This ratio is therefore about 1.13 for $\alpha = 1$, justifying the smaller flow rate of the rectangular duct. Moreover, as α increases, the perimeter ratio takes higher values, resulting in smaller flow rate ratios. The reason that the difference between the flow rates is increased by increasing n is that the velocity reduction within EDL is increased by increasing this parameter.

5 Conclusions

The pressure effects on the fully developed electroosmotic flow of power-law fluids in rectangular microchannels were studied in this paper. The electrical potential and momentum equations were numerically solved by means of a central finite difference scheme for a non-uniform grid. An extensive parametric study was performed in order to investigate the effects of the flow parameters on the hydrodynamic characteristics of the flow. It was observed that the pressure effects become more prominent at higher values of the channel aspect ratio. It was also found that a shear-thinning fluid, because of its nature, is more affected by the pressure gradient. The Poiseuille number was found to be an increasing function of the channel aspect ratio for pressure assisted flow and a slightly decreasing function for pressure opposed flow. It was also found that the Poiseuille number is an increasing function of the zeta potential. In addition, the results reveal that for shear-thinning fluids, the viscosity at the wall for pressure opposed flow case is higher than that of the pressure assisted flow

case, whereas the opposite trend is seen for shear thickenings. Moreover, the flow rate ratio, that is the flow rate divided by that of a Newtonian fluid at the same conditions, is a decreasing function of the flow behavior index, regardless of the other flow parameters. It is also found that whereas a higher flow rate ratio is obtained for shear-thinning fluids in the presence of a favorable pressure gradient as compared to that of an unfavorable pressure gradient, this trend is reversed for shear thickenings. Last but not least, a comparison of the results with those of the circular channels with the same cross-sectional area under pure effect of electroosmotic body force shows that the flow rate is lower for rectangular channels. The difference between the flow rates is observed to be pronounced by increasing the aspect ratio of the rectangular geometry and the flow behavior index.

References

1. Lemoff, A.V., Lee, A.P.: AC magnetohydrodynamic micropump. Sens. Actuators B: Chem. **63**(3), 178–185 (2000)
2. van Lintel, H.T.G., van De Pol, F.C.M., Bouwstra, S.: A piezoelectric micropump based on micromachining of silicon. Sens. Actuators **15**(2), 153–167 (1988)
3. Richter, A., Plettner, A., Hofmann, K.A., Sandmaier, H.: A micromachined electrohydrodynamic (EHD) pump. Sens. Actuators: A. Phys. **29**(2), 159–168 (1991)
4. Arulanandam, S., Li, D.: Liquid transport in rectangular microchannels by electroosmotic pumping. Colloids Surf. A: Physicochem. Eng. Aspects **161**(1), 89–102 (2000)
5. Reuss, F.F.: Charge-induced flow. Proc. Imp. Soc. Naturalists Moscow **3**, 327–344 (1809)
6. Burgreen, D., Nakache, F.R.: Electrokinetic flow in ultrafine capillary slits. J. Phys. Chem. **68**(5), 1084–1091 (1964)
7. Rice, C.L., Whitehead, R.: Electrokinetic flow in a narrow cylindrical capillary. J. Phys. Chem. **69**(11), 4017–4024 (1965)
8. Levine, S., Marriott, J.R., Neale, G., Epstein, N.: Theory of electrokinetic flow in fine cylindrical capillaries at high zeta-potentials. J. Colloid Interface Sci. **52**(1), 136–149 (1975)
9. Kang, Y., Yang, C., Huang, X.: Electroosmotic flow in a capillary annulus with high zeta potentials. J. Colloid Interface Sci. **253**(2), 285–294 (2002)
10. Yang, D.: Analytical solution of mixed electroosmotic and pressure-driven flow in rectangular microchannels. Key Eng. Mater. **483**, 679–683 (2011)
11. Wang, C.Y., Liu, Y.H., Chang, C.C.: Analytical solution of electro-osmotic flow in a semicircular microchannel. Phys. Fluids **20**(6), 063105 (2008)
12. Das, S., Chakraborty, S.: Analytical solutions for velocity, temperature and concentration distribution in electroosmotic microchannel flows of a non-Newtonian bio-fluid. Analytica Chimica Acta **559**(1), 15–24 (2006)
13. Zhao, C., Zholkovskij, E., Masliyah, J., Yang, C.: Analysis of electroosmotic flow of power-law fluids in a slit microchannel. J. Colloid Interface Sci. **326**(2), 503–510 (2008)
14. Zhao, C., Yang, C.: Nonlinear Smoluchowski velocity for electroosmosis of power-law fluids over a surface with arbitrary zeta potentials. Electrophoresis **31**(5), 973–979 (2010)
15. Zhao, C., Yang, C.: Electroosmotic flows of non-Newtonian power-law fluids in a cylindrical microchannel. Electrophoresis **34**(5), 662–667 (2013)
16. Vasu, N., De, S.: Electroosmotic flow of power-law fluids at high zeta potentials. Colloids Surf. A: Physicochem. Eng. Aspects **368**(1–3), 44–52 (2010)
17. Bandopadhyay, A., Chakraborty, S.: Steric-effect induced alterations in streaming potential and energy transfer efficiency of non-newtonian fluids in narrow confinements. Langmuir **27**(19), 12243–12252 (2011)
18. Deng, S.Y., Jian, Y.J., Bi, Y.H., Chang, L., Wang, H.J., Liu, Q.S.: Unsteady electroosmotic flow of power-law fluid in a rectangular microchannel. Mech. Res. Commun. **39**(1), 9–14 (2012)
19. Vasu, N., De, S.: Electroviscous effects in purely pressure driven flow and stationary plane analysis in electroosmotic flow of power-law fluids in a slit microchannel. Int. J. Eng. Sci. **48**(11), 1641–1658 (2010)
20. Bharti, R.P., Harvie, D.J.E., Davidson, M.R.: Electroviscous effects in steady fully developed flow of a power-law liquid through a cylindrical microchannel. Int. J. Heat Fluid Flow **30**(4), 804–811 (2009)
21. Park, H.M., Lee, W.M.: Helmholtz–Smoluchowski velocity for viscoelastic electroosmotic flows. J. Colloid Interface Sci. **317**(2), 631–636 (2008)
22. Park, H.M., Lee, W.M.: Effect of viscoelasticity on the flow pattern and the volumetric flow rate in electroosmotic flows through a microchannel. Lab Chip-Miniaturisation Chem. Biol. **8**(7), 1163–1170 (2008)
23. Dhinakaran, S., Afonso, A.M., Alves, M.A., Pinho, F.T.: Steady viscoelastic fluid flow between parallel plates under electro-osmotic forces: Phan–Thien–Tanner model. J. Colloid Interface Sci. **344**(2), 513–520 (2010)
24. Afonso, A.M., Alves, M.A., Pinho, F.T.: Analytical solution of mixed electro-osmotic/pressure driven flows of viscoelastic fluids in microchannels. J. Non-Newtonian Fluid Mech. **159**(1–3), 50–63 (2009)
25. Afonso, A.M., Alves, M.A., Pinho, F.T.: Electro-osmotic flow of viscoelastic fluids in microchannels under asymmetric zeta potentials. J. Eng. Math. **71**(1), 15–30 (2011)
26. Babaie, A., Sadeghi, A., Saidi, M.H.: Combined electroosmotically and pressure driven flow of power-law fluids in a slit microchannel. J. Non-Newtonian Fluid Mech. **166**(14–15), 792–798 (2011)
27. Babaie, A., Saidi, M.H., Sadeghi, A.: Electroosmotic flow of power-law fluids with temperature dependent properties. J. Non-Newtonian Fluid Mech. **185–186**, 49–57 (2012)
28. Sousa, J.J., Afonso, A.M., Pinho, F.T., Alves, M.A.: Effect of the skimming layer on electro-osmotic-Poiseuille flows of viscoelastic fluids. Microfluid. Nanofluidics **10**(1), 107–122 (2011)
29. Vakili, M.A., Sadeghi, A., Saidi, M.H., Mozafari, A.A.: Electrokinetically driven fluidic transport of power-law fluids in rectangular microchannels. Colloids Surf. A: Physicochem. Eng. Aspects **414**, 440–456 (2012)

30. Probstein, R.F.: Physicochemical Hydrodynamics. 2nd edn. Wiley, New York (1994)
31. Yang, C., Li, D., Masliyah, J.H.: Modeling forced liquid convection in rectangular microchannels with electrokinetic effects. Int. J. Heat Mass Transf. **41**(24), 4229–4249 (1998)
32. Deen, W.M.: Analysis of Transport Phenomena. Oxford University Press, New York (1998)
33. Dutta, D.: Electroosmotic transport through rectangular channels with small zeta potentials. J. Colloid Interface Sci. **315**(2), 740–746 (2007)
34. Moghadam, A.J.: Electrokinetic-driven flow and heat transfer of a non-newtonian fluid in a circular microchannel. J. Heat Transf. **135**(2), 021705 (2013)